

Novel Small Molecule Fibroblast Growth Factor 23 Inhibitors Increase Serum Phosphate and Improve Skeletal Abnormalities in *Hyp* Mice^S

Zhousheng Xiao, Jiawang Liu, Shih-Hsien Liu, Loukas Petridis, Chun Cai, Li Cao, Guangwei Wang, Ai Lin Chin, Jacob W. Cleveland, Munachi O. Ikedionwu, Jesse D. Carrick, Jeremy C. Smith, and Leigh Darryl Quarles

Department of Medicine, College of Medicine (Z.X., C.C., L.C., G.W.W., L.D.Q.) and Department of Pharmaceutical Sciences, College of Pharmacy (J.L.), University of Tennessee Health Science Center, Memphis, Tennessee; University of Tennessee (UT)/ Oak Ridge National Laboratory (ORNL) Center for Molecular Biophysics, Oak Ridge National Laboratory, Oak Ridge, Tennessee (S.H.L., L.P., J.C.S.); Department of Biochemistry and Cellular and Molecular Biology, University of Tennessee, Knoxville, Tennessee (L.P., J.C.S.); and Department of Chemistry, Tennessee Technological University, Cookeville, Tennessee (A.L.C., J.W.C., M.O.I., J.D.C.)

Received December 8, 2021; accepted March 20, 2022

ABSTRACT

Excess fibroblast growth factor (FGF) 23 causes hereditary hypophosphatemic rickets, such as X-linked hypophosphatemia (XLH) and tumor-induced osteomalacia (TIO). A small molecule that specifically binds to FGF23 to prevent activation of the fibroblast growth factor receptor/ α -Klotho complex has potential advantages over the currently approved systemically administered FGF23 blocking antibody. Using structure-based drug design, we previously identified ZINC13407541 (N-[[2-(2-phenylethenyl)cyclopenten-1-yl]methylidene]hydroxylamine) as a small molecule antagonist for FGF23. Additional structure-activity studies developed a series of ZINC13407541 analogs with enhanced drug-like properties. In this study, we tested in a preclinical *Hyp* mouse homolog of XLH a direct connect analog [(E)-2-(4-(*tert*-butyl)phenyl)cyclopent-1-ene-1-carbaldehyde oxime] (**8n**), which exhibited the greatest stability in microsomal assays, and [(E)-2-(E-4-methylstyryl)benzaldehyde oxime] (**13a**), which exhibited increased in vitro potency. Using cryo-electron microscopy structure and computational docking, we identified a key binding residue (Q156) of the FGF23 antagonists, ZINC13407541, and its analogs (**8n** and **13a**) in the N-terminal domain of FGF23 protein. Site-directed mutagenesis and bimolecular fluorescence complementation-fluorescence resonance energy transfer assay confirmed the binding site of these three antagonists. We found

that pharmacological inhibition of FGF23 with either of these compounds blocked FGF23 signaling and increased serum phosphate and 1,25-dihydroxyvitamin D [$1,25(\text{OH})_2\text{D}$] concentrations in *Hyp* mice. Long-term parenteral treatment with **8n** or **13a** also enhanced linear bone growth, increased mineralization of bone, and narrowed the growth plate in *Hyp* mice. The more potent **13a** compound had greater therapeutic effects in *Hyp* mice. Further optimization of these FGF23 inhibitors may lead to versatile drugs to treat excess FGF23-mediated disorders.

SIGNIFICANCE STATEMENT

This study used structure-based drug design and medicinal chemistry approaches to identify and optimize small molecules with different stability and potency, which antagonize excessive actions of fibroblast growth factor 23 (FGF23) in hereditary hypophosphatemic rickets. The findings confirmed that these antagonists bind to the N-terminus of FGF23 to inhibit its binding to and activation of the fibroblast growth factor receptors/ α -Klotho signaling complex. Administration of these lead compounds improved phosphate homeostasis and abnormal skeletal phenotypes in a preclinical *Hyp* mouse model.

Introduction

Fibroblast growth factor 23 (FGF23) is a hormone produced by osteoblasts/osteocytes in the bone, which activates the FGF

receptor/ α -Klotho (α -KL) binary receptor complex in renal proximal tubules to regulate phosphate reabsorption and $1,25(\text{OH})_2\text{D}$ metabolism and in distal tubules to adjust sodium and calcium reabsorption (Quarles, 2003, 2011). FGF23 plays a causal role in hereditary hypophosphatemic disorders, such as X-linked hypophosphatemia (XLH) and autosomal recessive hypophosphatemia rickets and acquired tumor-induced osteomalacia (TIO). Elevated FGF23 plays an adaptive role in maintaining phosphate homeostasis in chronic kidney disease but is also associated with left ventricular hypertrophy and increased cardiovascular mortality in this setting (Gutierrez et al., 2008, 2009; Hsu and Wu, 2009; Jean et al., 2009; Isakova et al., 2011).

This work was supported by National Institutes of Health National Institute of Diabetes and Digestive and Kidney Diseases [Grant R01-DK121132] (to L.D.Q.) and the Compute and Data Environment for Science at the Oak Ridge National Laboratory, which is supported by the Office of Science of the U.S. Department of Energy [Contract DE-AC05-00OR22725].

No author has an actual or perceived conflict of interest with the contents of this article.

A preprint of this article was deposited in bioRxiv [https://doi.org/10.1101/2020.08.04.236877].

dx.doi.org/10.1124/molpharm.121.000471.

^S This article has supplemental material available at molpharm.aspetjournals.org.

Until recently, treatment of hereditary FGF23-mediated hypophosphatemic disorders consisted of 1,25(OH)₂D and phosphate supplements. This approach does not cure the disease and is associated with toxicities related to excess phosphate and 1,25(OH)₂D, including nephrocalcinosis (Colares Neto et al., 2019; Arango Sancho, 2020). TIO can be cured by resection of the tumor that is producing FGF23, but surgical removal of the tumor is not possible in approximately 50% of these patients (Fukumoto, 2014; Florenzano et al., 2017).

An FGF23 blocking antibody KRN23 (Burosumab, a human monoclonal IgG1 antibody targeting FGF23 and developed by Kyowa Hakko Kirin and Ultragenyx) has been recently approved for the treatment of XLH and TIO by the U.S. Food and Drug Administration (Carpenter et al., 2018; Lamb, 2018). KRN23 subcutaneously administered at an average dose of 0.98 mg/kg every 2 weeks improves rickets and increases serum phosphate levels in XLH (Carpenter et al., 2014), and was superior to conventional treatment with phosphate and 1,25(OH)₂D supplements. To date, KRN23 has not been associated with toxicity at the doses used to treat hypophosphatemia, but the initial use of a high affinity FGF23 blocking antibody in preclinical rodent models resulted in

excess mortality (Shalhoub et al., 2012), principally due to oversuppression of FGF23 and resulting hyperphosphatemia and 1,25(OH)₂D toxicity (Stubbs et al., 2007; Yamazaki et al., 2008; Fukumoto, 2018). Additional disadvantages of KRN23 include the need for systemic administration, long half-life (elimination half-life of 18 days), and cost.

A small molecule drug to block FGF23 activation of the FGFRs/ α -Klotho receptor would have several potential advantages over KRN23. We used homology modeling, molecular dynamics simulation, and virtual high-throughput screening to identify ZINC13407541 (N-[[2-(2-phenylethenyl)cyclopenten-1-yl]methylidene]hydroxylamine), which binds to FGF23 and inhibits FGF23 interaction with FGFRs (Xiao et al., 2016). The core ZINC13407541 structure contains two ring systems, bridged with an ethylene, and a carbaldehyde oxime functional group on the *ortho*- position of ring A that is essential for activity (Fig. 1). Subsequent medicinal chemistry investigation of structure-activity relationships based on ZINC13407541 produced 36 analogs with different stabilities and potencies (Downs et al., 2021). Of these, the **13a** analog, created by replacing a five-membered aliphatic ring A with a six-membered ring and substituting a *para*-position hydrogen atom on the aryl ring B with electron-

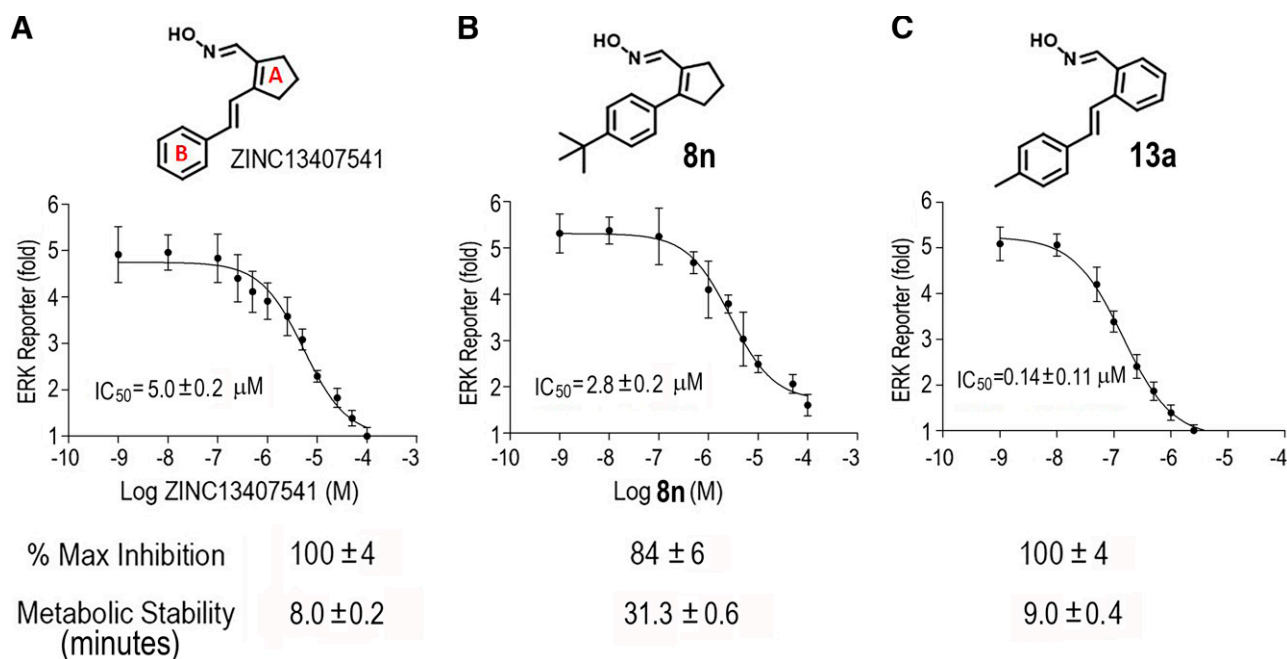


Fig. 1. Structure, in vitro efficacy, and metabolic stability of ZINC13407541 (A) and its analogs **8n** (B) and **13a** (C). IC₅₀ values were extracted from three independent concentration-response experiments examining the compound-dependent inhibition of FGF23-induced ERK reporter activities in HEK293T cells expressing human α -KL after application of ZINC13407541 ($n = 3$ cells) and its analogs **8n** ($n = 3$ cells) and **13a** ($n = 3$ cells). Maximum percent inhibition values were calculated from the plateaus in inhibition at the highest inhibitor concentration ($n = 3$ cells for each compound). Metabolic stabilities were expressed as the half-life of the parent compound remaining after an incubation with human liver microsomes ($n = 3$ liver microsomes for each compound).

ABBREVIATIONS: **13a**, [(E)-2-((E)-4-methylstyryl)benzaldehyde oxime]; ALP, alkaline phosphatase; BiFC, bimolecular fluorescence complementation; BMD, bone mineral density; CFP, cyan fluorescent protein; CKD, chronic kidney disease; Ct, threshold cycle; Ct.Th, cortical thickness; Cyp, cytochrome P450; 3D, three-dimensional; Dmp1, Dentin matrix protein 1; ERK, extracellular signal-regulated kinase; FGF, fibroblast growth factor; FGFR, fibroblast growth factor receptor; FRET, fluorescence resonance energy transfer; Gln, glutamine; HEK293T, human embryonic kidney 293 cells transformed with large T antigen; α -KL, α -Klotho; MEPE, matrix extracellular phosphoglycoprotein; **8n**, [(E)-2-(4-(*tert*-butyl)phenyl)cyclopent-1-ene-1-carbaldehyde oxime]; NCC, sodium-chloride co-transporter; Npt, sodium phosphate co-transporter; 1,25(OH)₂D, 1,25-dihydroxyvitamin D; 25(OH)D, 25-hydroxyvitamin D; PDB, protein data bank; PTH, parathyroid hormone; RT-PCR, reverse-transcription polymerase chain reaction; TIO, tumor-induced factor osteomalacia; VC155, C-terminal fragment of Venus (residues 155–238); VN155, N-terminal fragment of Venus (residues 1–154); Wnt, wingless; XLH, X-linked hypophosphatemia; YFP, yellow fluorescent protein; ZINC13407541, N-[[2-(2-phenylethenyl)cyclopenten-1-yl]methylidene]hydroxylamine.

donating a methyl group (CH₃), markedly increases potency of the FGF23 antagonists. The analog **8n**, created by eliminating the ethylene bridge between the two ring systems of ZINC13407541 to create a direct connect derivative, decreased efficacy but increased metabolic stability (Downs et al., 2021).

In this study, we refined the docking of these compounds to FGF23 three-dimensional (3D) structural data (Chen et al., 2018), performed mutagenesis and fluorescence resonance energy transfer (FRET) analysis to confirm binding of the antagonists to FGF23, and tested the *in vivo* efficacy of the most potent compound, **13a**, in the preclinical *Hyp* mouse model of XLH.

Materials and Methods

Molecular Docking of Experimentally Verified Hits on the N-Terminal Domain of FGF23. To computationally analyze the binding conformation and affinity of ZINC13407541 and its two analogs, **13a** and **8n**, to FGF23, molecular docking of the three compounds to the crystal structure of FGF23 [Protein Data Bank (PDB) code: 5W21 (Chen et al., 2018)] and its Q156A mutant (Webb and Sali, 2014) was performed using AutoDock VinaMPI (Trott and Olson, 2010; Ellingson et al., 2013). A rectangular box of 40 × 30 × 40 Å (X × Y × Z directions) was geometrically centered at 88.37, 120.84, 60.25 Å to include the whole N-terminal domain of FGF23, and the entire box was used for searching ligand poses. An exhaustiveness of 30 was used for adequate sampling of ligand conformations within the box, and 20 binding poses were considered for each of the three compounds to wild-type FGF23. The files in PDB format of FGF23 and all poses in the docking are included in the “supplemental data files–PDB files” and their captions are included in the “supplemental file” as supporting information. After docking, each pose *i* of a compound was given a Boltzmann weight (Widom, 2002) W_i :

$$W_i = \frac{\exp\left(\frac{-\Delta G_i}{k_B T}\right)}{\sum_{i=1}^{20} \exp\left(\frac{-\Delta G_i}{k_B T}\right)} \quad (1)$$

where ΔG_i is the estimated free energy of binding for pose *i*, k_B is Boltzmann constant, and *T* is human body temperature at 310 K. The hydrogen-bond analyses were performed on each pose *i* using LigPlot⁺ (Laskowski and Swindells, 2011) along with W_i to give each residue on FGF23 a weighted hydrogen-bond score *H*:

$$H = \sum_{i=1}^{20} H_i W_i \quad (2)$$

where H_i is the number of hydrogen bonds between pose *i* of the ligand and the residue. For hydrogen-bond calculation in LigPlot⁺ (Laskowski and Swindells, 2011), the maximum hydrogen-acceptor and maximum donor-acceptor distances were set at 3.0 and 4.0 Å, respectively. For residues whose *H* were not zero, each of them was given an estimated conservation score using The ConSurf Server (<https://consurf.tau.ac.il/>) (Ashkenazy et al., 2016) with default settings. Among the three compounds, the consensus residue with the highest *H* and conservation score was chosen as the potential binding site. Subsequently, the pose with hydrogen bonding to the potential binding site and with the lowest ΔG for each compound was plotted in three and two dimensions using visual molecular dynamics (VMD) (Humphrey et al., 1996) and LigPlot⁺ (Laskowski and Swindells, 2011), respectively. For nonbonded contact calculation in LigPlot⁺ (Laskowski and Swindells, 2011), the minimum and maximum contact distances were set at 2.0 and 4.0 Å, respectively. Dissociation constant (K_d) and machine deep learning (K_{DEEP}) software (Jiménez et al., 2018), a protein-ligand absolute binding affinity predictor based on deep convolutional neural networks, was also used to obtain ΔG for the plotted pose of each compound as a comparison

with AutoDock VinaMPI (Trott and Olson, 2010; Ellingson et al., 2013).

Chemicals and Reagents. Synthetic preparation of new ZINC13407541 analogs was conducted in the medicinal chemistry laboratory at University of Tennessee Health Science Center College of Pharmacy and Tennessee Technological University. All reagents used for organic synthesis were sourced from Sigma-Aldrich (St. Louis, MO) and Fisher Scientific (Fairfield, NJ), and stored in accordance with manufacturer recommendations. Each test compound was fully characterized by mass spectrometry and NMR (¹H and ¹³C), with a >95% chemical purity which was determined with high-performance liquid chromatography (HPLC). The medicinal chemistry group also generated gram-scale quantities for *in vivo* animal studies as we previously reported (Xiao et al., 2016). The compounds were stored at −20°C and tested both *in vitro* assays and *in vivo* in the laboratories. Recombinant human FGF23 protein (2604-FG-025) was purchased from R&D Systems (Minneapolis, MN).

Cell Culture and In Vitro Functional Assays. Human embryonic kidney 293 cells transformed with large T antigen (HEK293T) were cultured in Dulbecco's modified Eagle's medium containing 10% FBS and 1% penicillin and streptomycin. To test the effects of the novel compounds on FGF23-mediated activation of FGFR1/α-KL complex, HEK293T cells were transiently transfected with either empty expression vector or full-length human α-KL along with the extracellular signal-regulated kinase (ERK) luciferase reporter system (Urakawa et al., 2006) and *Renilla* luciferase-null as internal control plasmid. Transfections were performed by electroporation using Cell Line Nucleofector Kit R according to the manufacturer's protocol (Amaxa, Inc., Gaithersburg, MD). Thirty-six hours after transfection, the transfected cells were treated with the test compound with a range of 10^{−9}~10^{−4} M in the presence or absence of 1 nM FGF23. After 5 hours, the cells were lysed and luciferase activities measured using a Synergy H4 Hybrid Multi-Mode Microplate Reader (Winooski, VT) and Promega Dual-Luciferase Reporter Assay System (Madison, WI).

In Vitro Absorption, Distribution, Metabolism, and Excretion Studies. We contracted the *in vitro* absorption, distribution, metabolism, and excretion screening with Eurofins Pharma Discovery Services. Microsomal stability of ZINC13407541 and ZINC13407541 analogs was determined in liver microsomes, including human liver microsomes and mouse liver microsomes to determine potential species differences in metabolism (Zeng et al., 2011). Aqueous solubility was assessed in PBS (pH 7.4), simulated intestinal fluid, and simulated gastric fluid. We also extended our assessment of compound *in vitro* absorption, distribution, metabolism, and excretion by assessing protein binding, permeability, and metabolism. We assessed protein binding using rapid equilibrium dialysis, as previously described (Song et al., 2008).

RNA Purification and Quantitative Real-Time Reverse-Transcription Polymerase Chain Reaction. For quantitative real-time reverse-transcription polymerase chain reaction (RT-PCR), 1.0 μg total RNA isolated from heart, kidney, or long bone of 8-week-old mice was reverse transcribed as previously described (Qiu et al., 2012a, 2012b). Polymerase chain reactions contained 100 ng template (cDNA or RNA), 300 nM each forward and reverse primers, and 1XqPCR Supermix (Bio-Rad, Hercules, CA) in 50 μl. The threshold cycle (C_t) of tested-gene product from the indicated genotype was normalized to the C_t for cyclophilin A. Expression of total *Klotho* isoform transcripts was performed using the following *Klotho*-isoform-specific primers: Forward primer of mouse *m-KL*¹³⁵ transcript: 5'-CAT TTC CCT GTG ACT TTG CTT G-3', and reverse primer: 5'-ATG CAC ATC CCA CAG ATA GAC-3'. Forward primer of mouse *s-KL*⁷⁰ transcript: 5'-GAG TCA GGA CAA GGA GCT GT-3', and reverse primer: 5'-GGC CGA CAC TGG GTT TTG-3'. The sequences of primers for kidney and bone gene transcripts were previously reported (Qiu et al., 2012a, Qiu et al., 2012b). In addition, the fold change of tested gene transcripts was calculated from the relative levels of the normal gene transcripts in wild-type mice.

Bimolecular Fluorescence Complementation-Fluorescence Resonance Energy Transfer and Site-Directed Mutagenesis Study. We used a bimolecular fluorescence complementation (BiFC)-based FRET assay to measure the interaction of FGF-23/FGFR1/ α -Klotho triple complexes in living cells (Shyu et al., 2008a, 2008b; Tian et al., 2007). For this, we used a FGFR1 and a α -Klotho cDNA construct fused to the N- and C-terminal nonfluorescent fragments of Venus [FGFR1-N-terminal fragment of Venus (residues 1–154, VN155) and α -Klotho-C-terminal fragment of Venus (residues 155–238, VC155)] and a FGF-23 cDNA construct fused to the full-length fluorescent protein Cerulean (Cerulean-FGF-23). The interaction between FGFR1-VN155 + α -Klotho-VC155 proteins reconstitutes an intact Venus (FGFR1-VN155/ α -Klotho-VC155 dimer complexes), which serves as a FRET acceptor molecule. The FGF-23/FGFR1/ α -Klotho triple complex formation brings Cerulean-FGF-23 (FRET donor) in proximity to the reconstituted Venus (FGFR1-VN155/ α -Klotho-VC155 dimer complexes), allowing FRET to take place. For BiFC-based FRET assays, the HEK-293T cells will be cotransfected with Cerulean-FGF-23, FGFR1-VN155, and α -Klotho-VC155 constructs. The formation of FGFR1-VN155/ α -Klotho-VC155 dimer complexes allows the FRET signal to be detected when a donor excitation (Cerulean-FGF-23) is applied. The HEK293 cells cultured in 96-well plates were treated with various compounds for 60 minutes. At the indicated time point, the emission signals of yellow fluorescent protein (YFP) (535 ± 8 nm) and cyan fluorescent protein (CFP) (486 ± 8 nm) were respectively measured by a Synergy H4 plate reader using an excitation light of 440 ± 10 nm. The background fluorescence was then measured from the wells containing only medium. After subtracting the background fluorescence from the recorded signal, net YFP and CFP readings were obtained. In this document, YFP/CFP emission ratio is used to represent the effect of FRET, which is equal to the net YFP reading divided by the net CFP reading from the same well. In addition, based on the identification of crucial contact residues that inhibit FGF-23 activity in the above computational modeling, we used a Q5 site-directed mutagenesis kit to generate amino-acid residue substitutions at the interaction sites (Q156A) in *wild-type* Cerulean-FGF-23WT cDNA to create mutant constructs (Cerulean-FGF-23Q156A) that disrupt the contact sites in small chemical/FGF-23 binding pocket of *wild-type* FGF-23. Then we used the same approach to cotransfect either Cerulean-FGF-23WT or Cerulean-FGF-23Q156A along with FGFR1-VN155 and α -Klotho-VC155 constructs into HEK293 cells to measure the changes of YFP/CFP emission ratio as well as the ERK luciferase reporter activities after treated with various compounds.

Animal Experiments. All animal research was conducted according to guidelines provided by National Institutes of Health and the Institute of Laboratory Animal Resources, National Research Council. The University of Tennessee Health Science Center's Animal Care and Use Committee approved all animal studies (Protocol number: 18-111.0). All mice were maintained in our vivarium on a standard diet (7912; Harlan Teklad, Madison, WI). To generate hemizygous *Hyp* mice, we crossed male hemizygous with female *wild-type* to obtain both male and female hemizygous *Hyp* mice as previously described (Xiao et al., 2014). At 4 weeks of age, hemizygous *Hyp* mice were randomly assigned to the following experiments. We excluded the individual *Hyp* mice at extremes of the stated age range. For single-dose experiment, the 6-week-old *Hyp* mice received a single i.p. dose of ZINC13407541 (0, 50, 100, 200 mg/kg) or **13a** (0, 10, 50, 100 mg/kg) at time 0 and were collected serum samples 0, 2, 4, 8, and 24 hours after administration. For short-term efficacy studies, the 6-week-old *Hyp* mice were divided into four different groups: (1) Vehicle control; (2) ZINC13407541 (100 mg/kg); (3) **8n** (100 mg/kg); and (4) **13a** (100 mg/kg). The mice were treated with intraperitoneal injection of either vehicle control (5% DMSO in corn oil), or ZINC13407541, or **8n**, or **13a** twice a day for 3 days. For long-term treatments, the *Hyp* mice were divided into four different groups: (1) Vehicle control; (2) ZINC13407541 (50 mg/kg); (3) **8n** (50 mg/kg); and (4) **13a** (50 mg/kg). The 4-week-old *Hyp* mice were treated with intraperitoneal injection of either vehicle control (5% DMSO in corn oil), or ZINC13407541, or **8n**, or **13a** twice a day for four weeks. We assessed the effects of the

compounds on the skeletal phenotype at 8 weeks of age (after 4 weeks of treatment) using the methods previously described in studies that characterize the in vivo phenotypes of *Hyp* mice (Xiao et al., 2014). The serum samples were collected 4 hours after last dose administration. Serum FGF23 levels were measured using the FGF23 ELISA kit (Kainos Laboratories, Tokyo, Japan). Serum phosphorus levels were measured using a Phosphorus Liqui-UV kit (Stanbio Laboratories, Boerne, TX), and serum calcium levels were measured using a Calcium (CPC) Liquicolor kit (Stanbio Laboratories, Boerne, TX). Serum parathyroid hormone (PTH) levels were measured using the Mouse Intact PTH ELISA kit (Immutopics, Carlsbad, CA). Serum aldosterone levels were measured using aldosterone ELISA Kit (Cayman Chemical, MI). Serum 1,25(OH)₂D levels were measured using the 1,25-dihydroxy-vitamin D ELA Kit (Immunodiagnostic Systems, Fountain Hills, AZ) as previously described (Xiao et al., 2014).

Bone Densitometry, Histomorphometric, and Micro-Computed Tomography Analysis. Bone mineral density (BMD) of femurs was assessed at 8 weeks of age using a small animal bone densitometer (Lunar Corp, Madison, WI). Calcein (Sigma-Aldrich, St. Louis, MO) double labeling of bone and histomorphometric analyses of periosteal mineral apposition rate in tibias were performed using the osteomeasure analysis system (Osteometrics, Inc., Decatur, GA). The distal femoral metaphyses were also scanned using a micro-computed tomography (CT) 40 scanner (Scanco Medical AG, Brüttisellen, Switzerland). A 3D images analysis was done to determine width of growth plate, bone volume, and cortical thickness (Ct.Th) as previously described (Xiao et al., 2008; Xiao et al., 2010).

Statistical Analysis. We evaluated differences between two groups by unpaired *t* test, multiple groups by one-way analysis of variance, and two groups over time by two-way analysis of variance with interactions. All values are expressed as means \pm S.D. All computations were performed using a commercial biostatistics software (GraphPad Software Inc. La Jolla, CA).

TABLE 1

The weighted hydrogen-bond scores *H* (see eqs. 1 and 2 for details) in descending order for residues in the N-terminal domain of FGF23 that form hydrogen bonds with ZINC13407541, **13a**, and **8n** in the molecular docking

ZINC13407541		13a		8n	
Residue	<i>H</i>	Residue	<i>H</i>	Residue	<i>H</i>
Gln156	0.417	Tyr93	0.293	Tyr93	0.159
Asn122	0.408	Gln156	0.278	Gln156	0.143
Arg76	0.242	Asn122	0.207	Thr86	0.096
Ser77	0.159	Thr86	0.120	Tyr154	0.091
Tyr93	0.134	Arg76	0.113	Ser137	0.074
Thr86	0.115	Ser77	0.101	Gly139	0.074
Met74	0.083	Met74	0.078	Thr46	0.063
Val84	0.083	Val84	0.078	Asn49	0.063
Leu146	0.027	Ala45	0.035	Ser77	0.063
Ile75	0.024	Gln67	0.031	Arg76	0.061
Gly38	0.012	Leu146	0.021	Ser155	0.052
Glu78	0.009	Asn49	0.015	Ile75	0.047
Ser159	0.009	Pro152	0.015	Leu146	0.045
Gln118	0.007	Tyr154	0.015	Met74	0.033
Thr119	0.007	Ser155	0.015	Val84	0.033
				Ser34	0.024
				Gly38	0.024
				Pro152	0.024
				Asn162	0.024
				Ile164	0.024
				Asp125	0.020
				Tyr127	0.020
				Ser159	0.020

Ala, Alanine; Arg, Arginine; Asn, Asparagine; Asp, Aspartic acid; Glu, Glutamic acid; Gly, Glycine; Ile, Isoleucine; Leu, Leucine; Met, Methionine; Pro, Proline; Ser, Serine; Thr, Threonine; Tyr, Tyrosine; Val, Valine.

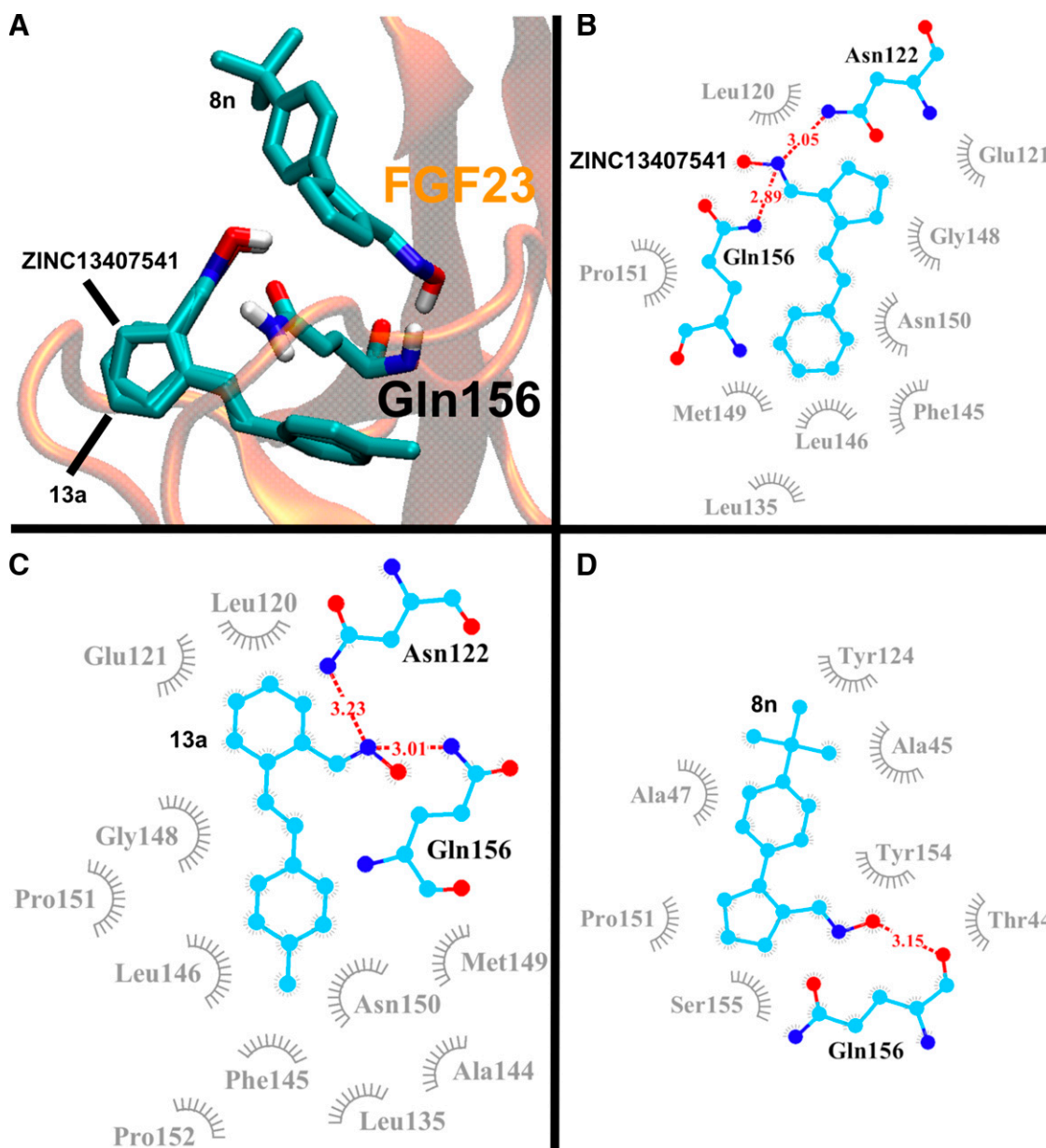


Fig. 2. The computationally predicted interaction of ZINC13407541 and its two analogs, **13a** and **8n**, with Gln156, the potential binding site, in the N-terminal domain of FGF23 (PDB code: 5W21) shown in (A) 3D structure; (B–D) two-dimensional residue-contacting map for ZINC13407541, **13a**, and **8n**, respectively. Hydrogen bonds are shown in red dash lines with donor-acceptor distances in Å. Hydrophobic interactions are shown in gray. The corresponding estimated free energies of binding (ΔG) for the three poses are shown in Table 2.

Results

We first investigated the in vitro metabolic stability and IC_{50} for the representative compounds. Compound **8n** and **13a** were identified from structure activity relationship studies of 36 newly synthesized compounds with different stability and potency in the in vitro assays (Downs et al., 2021). Compound **8n**, a direct connect analog of ZINC13407541 showed the greatest stability and **13a** the greatest potency of the 36 compounds generated. As shown in Fig. 1, compound **8n** has eliminated the ethylene bridge to form a directly connected two-ring scaffold, which decreased maximum inhibition activity (% maximum inhibition 84%), but showed increased potency IC_{50} (2.8 μM) and metabolic stability (31 minutes) compared with ZINC13407541 (100%, 5.0 μM , and 8 minutes).

In contrast, compound **13a** has exchanged the cyclopentene with a phenyl group, showing no changes in metabolic stability (9 minutes) and similar maximum inhibition activity (% maximum inhibition 100%), but 36-fold higher potency for

TABLE 2

Computationally estimated free energies of binding (ΔG) with standard errors for ZINC13407541, **13a**, and **8n** to Gln156 in the N-terminal domain of FGF23 using AutoDock VinaMPI and K_{DEEP} . The corresponding binding poses of ligands are shown in Fig. 2.

Compound	$\Delta G(\text{VinaMPI})$ [kcal/mol]	$\Delta G(K_{DEEP})$ [kcal/mol]
ZINC13407541	-7.0 ± 2.9	-6.4 ± 0.3
13a	-7.3 ± 2.9	-6.9 ± 0.5
8n	-5.8 ± 2.9	-4.9 ± 0.6

inhibiting FGF23 activity (**13a**, $IC_{50} = 0.14 \mu M$) compared with ZINC13407541 ($IC_{50} = 5.0 \mu M$).

We also performed the molecular docking of experimentally verified hits on the N-terminal domain of FGF23. Hydrogen-bond analyses after molecular docking (See Supplemental Tables 1–3 for results of the three compounds, ZINC13407541, and its two analogs, **13a** and **8n**) indicate that Gln156 is a consensus binding site in the N-terminal domain of FGF23 (Table 1). Moreover, Glutamine 156 (Gln156) is highly evolutionarily conserved (See Supplemental Table 4). Therefore, Gln156 may well be a binding site for the three compounds in experiments. Fig. 2A shows that ZINC13407541 and **13a** adopt similar poses. Further, ZINC13407541 and **13a** (See Fig. 2, B and C, respectively) each has two hydrogen bonds with Gln156 and Asparagine 122 (Asn122), and **8n** (Fig. 2D) has one hydrogen bond with Gln156. shows the estimated free energies of binding (ΔG) of the three compounds to FGF23, calculated using two different methods: AutoDock VinaMPI (Trott and Olson, 2010; Ellingson et al., 2013) and K_{DEEP} (Jiménez et al., 2018). The values ΔG (Trott and Olson, 2010; Jiménez et al., 2018) suggest that these three compounds bind to Gln156 on FGF23 with similar binding affinities. In addition, molecular docking of the three compounds to the N-terminal domain of FGF23 Q156A mutant shows that all the compounds no longer interact with Q156A (Supplemental Fig. 1) although ΔG of these compounds to the mutant (Supplemental Table 5) are similar to those to the wild-type (Table 2). This also suggests that Gln156 may be a key binding site.

We next validated key binding residue in FGF-23 protein through the BiFC-based FRET assays, ERK reporter activity, and site-directed mutagenesis. We generated FGFR1-VN155, α -Klotho-VC155, and Cerulean (CFP)-FGF-23 *wild-type* constructs (Fig. 3A) to create a BiFC-based FRET assay for measuring FGF23/FGFR1/ α -Klotho triple complex formation (Tian et al., 2007; Shyu et al., 2008a, 2008b). We also created a Cerulean (CFP)-FGF-23-Q156A mutant construct based on our molecular docking analysis above. We observed that ZINC13407541 reduced the YFP/CFP ratio at a concentration of $10 \mu M$. Compound **8n** ($10 \mu M$) had a similar effect as ZINC13407541. Compound **13a** ($5 \mu M$) exhibited an even greater effect on YFP/CFP ratio, indicating more complete disruption of FGF23/FGFR1/ α -Klotho triple complex formation (Fig. 3, B and D). In contrast, Q156A mutagenesis completely abolished the inhibition of YFP/CFP ratio by ZINC13407541 and its analogs (Fig. 3B). Mutagenesis alone had no effects on YFP/CFP ratio and FGF23/FGFR1/ α -Klotho triple complex formation (Fig. 3B). Consistent with the BiFC-based FRET data, the ERK reporter activity was not affected in mutant FGF23Q156A when compared with wild-type FGF23WT, suggesting that the Q156A mutation does not change the formation and function of the FGF23/FGFR1/ α -Klotho complex in an in vitro cell culture system. However, Q156A completely abolished the inhibition of the ERK reporter activity by ZINC13407541 ($10 \mu M$) and **8n** ($10 \mu M$). Compound **13a** ($5 \mu M$) thus inhibits FGF23Q156A-induced ERK reporter activity, indicating that **13a** may have other effects, such as solvation free energies of the isolated molecules or bind other proteins in the ERK signaling cascade (Fig. 3, C and D). These results suggest that Q156 is key binding residue in FGF-23 protein for ZINC13407541 and

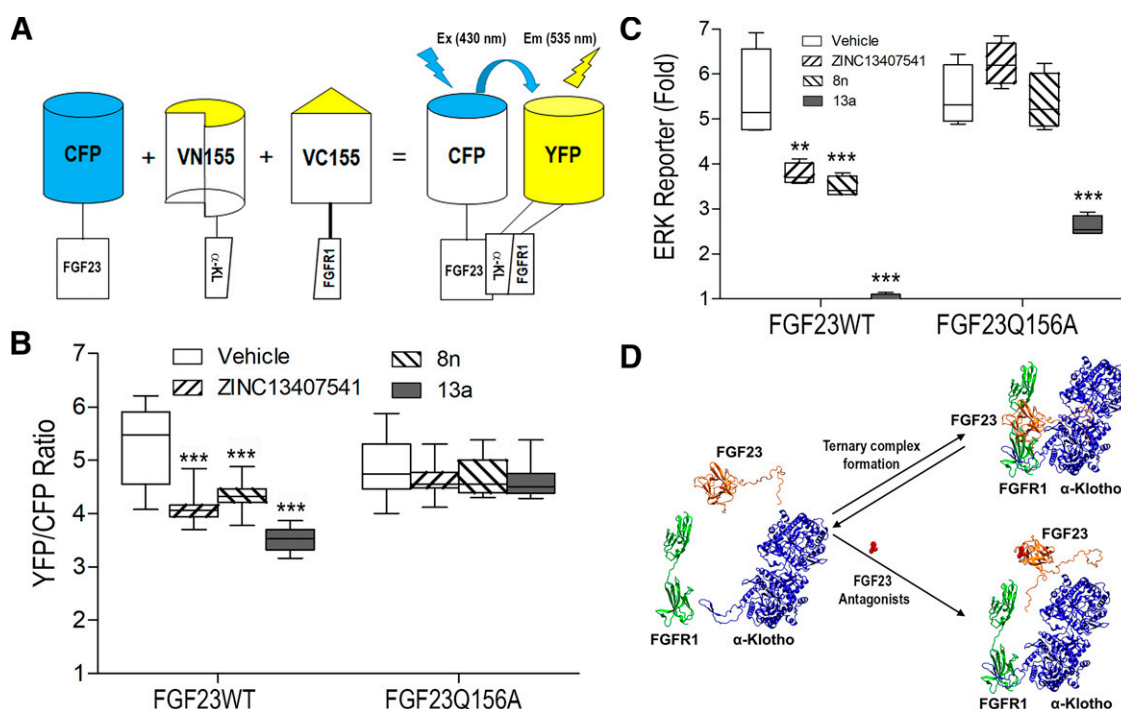


Fig. 3. Effects of ZINC13407541 and its analogs on CFP-FGF23WT or CFP-FGF23Q156A induced BiFC-based FRET ratio and ERK reporter activities. (A) Diagrams of fusion constructs for human CFP-FGF23WT, CFP-FGF23Q156A, α -KL-VN155, and FGFR1-VC155. (B) BiFC-based YFP/CFP ratio ($n = 3$ cells). (C) ERK reporter activities ($n = 3$ cells). (D) Computational model of FGF23 antagonist that targets FGF23/FGFR1/ α -Klotho complex. Data are expressed as the mean \pm S.D. from three independent experiments. *, **, and *** indicate statistically significant difference from vehicle control group. P values were determined by one-way ANOVA with Tukey's multiple-comparisons test.

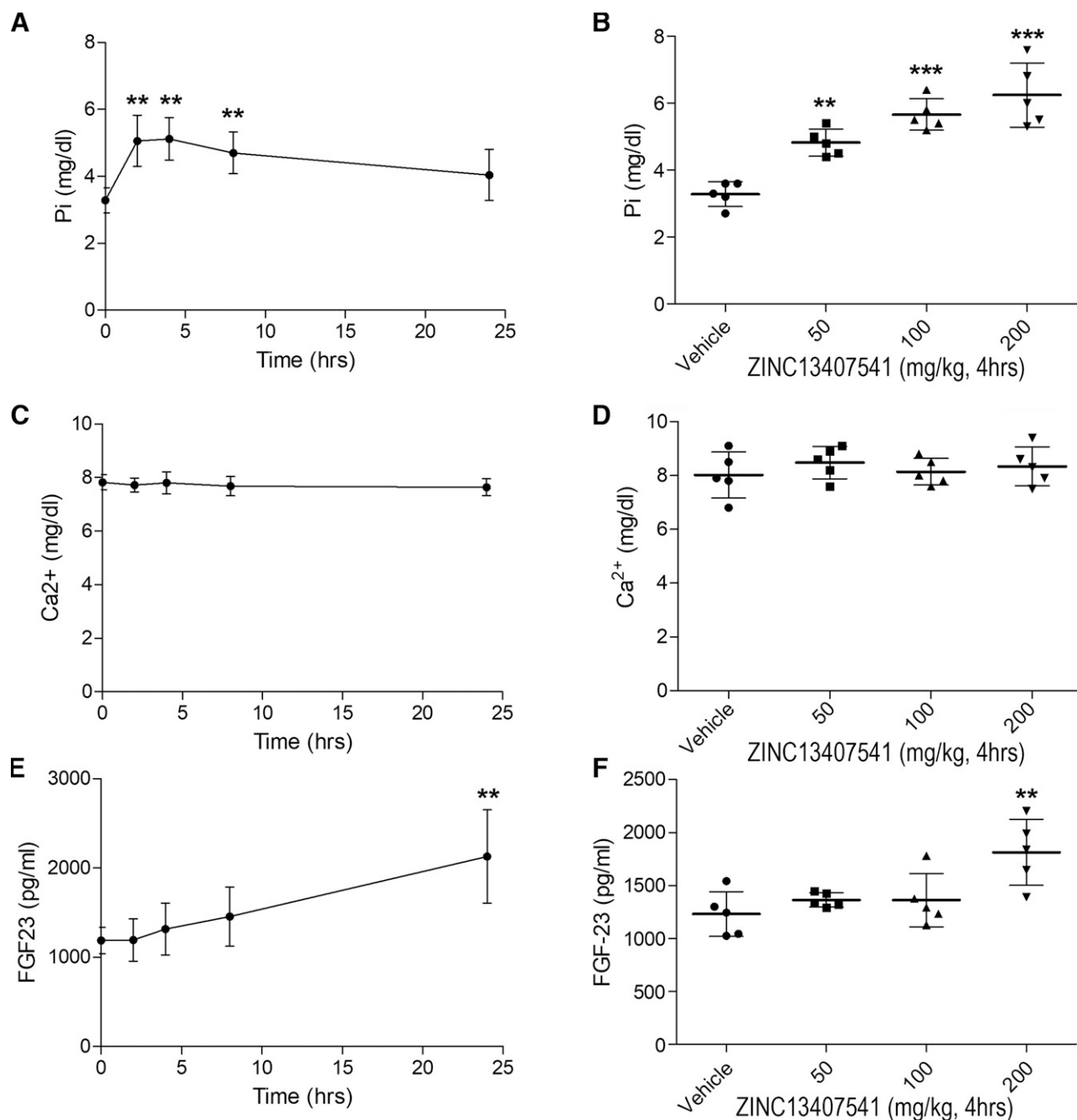


Fig. 4. Time- and dose-dependent effects of ZINC13407541 on mineral ion homeostasis and FGF23 levels in *Hyp* mice. In left panels (A), (C), and (E), time-course assessments of serum phosphate, calcium, and FGF23 levels in *Hyp* mice that were given a single i.p. injection of ZINC13407541 (100mg/kg) during 24 hours. In right panels (B), (D), and (F), dose-response studies of serum phosphate, calcium, and FGF23 levels in *Hyp* mice that were given a single i.p. injection of ZINC13407541 (50, 100, and 200 mg/kg) after 4 hours. Data are expressed as the mean \pm S.D. from serum samples of individual mice ($n = 5$). *, **, and *** indicate statistically significant difference from vehicle control group. P values were determined by 1-way ANOVA with Dunnett's test.

its analogs, and the compounds binding to FGF-23 protein disrupts FGF23/FGFR1/ α -Klotho triple complex conformation and its downstream signaling transduction (Fig. 3D).

To examine the *in vivo* efficacy of both **8n** and **13a** analogs compared with the parent molecule ZINC13407541 in preclinical animal studies, we measured the mineral ion homeostasis changes in serum of *Hyp* mice treated with

single-dose or short-term FGF23 inhibitors. In *Hyp* mice, a mouse homolog of XLH, administration of a single intra-peritoneal injection of ZINC13407541 (100 mg/kg) resulted in an increase in serum phosphate levels 2 hours after administration that peaked 4 hours after treatment and returned to original levels by 24 hours postinjection (Fig. 4, A and B). Also, the single IP injection of ZINC13407541

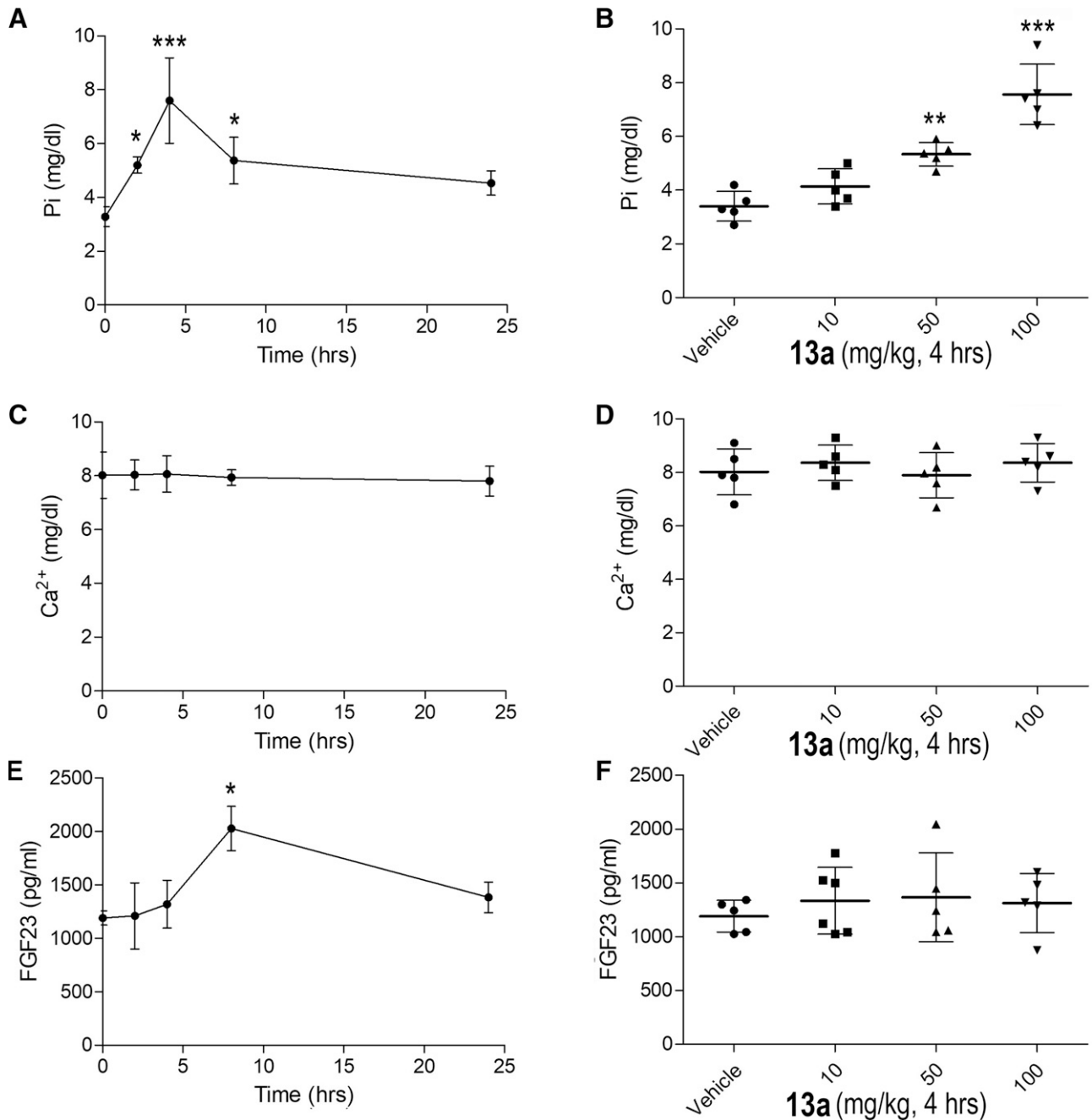


Fig. 5. Time- and dose-dependent effects of **13a** on mineral ion homeostasis and FGF23 levels in *Hyp* mice. In left panels (A), (C), and (E), time-course assessments of serum phosphate, calcium, and FGF23 levels in *Hyp* mice that were given a single i.p. injection of **13a** (100mg/kg) during 24 hours. In right panels (B), (D), and (F), dose-response studies of serum phosphate, calcium, and FGF23 levels in *Hyp* mice that were given a single i.p. injection of **13a** (10, 50, and 100 mg/kg) after 4 hours. Data are expressed as the mean \pm S.D. from serum samples of individual mice ($n = 5$). *, **, and *** indicate statistically significant difference from vehicle control group. P values were determined by one-way ANOVA with Dunnett's test.

increased *Hyp* mice serum phosphate levels in a dose-dependent manner, the maximum effect achieved in the dose of 200 mg/kg ZINC13407541 (Fig. 4, A and B). In contrast, the ZINC13407541 treatment did not affect serum calcium levels (Fig. 4, C and D). *Hyp* mice treated with 100 mg/kg dose of ZINC13407541 after 24 hours or with 200 mg/kg dosing of ZINC13407541 after 4 hours exhibited a twofold increase in serum FGF23 levels (Fig. 4, E and F). Compound **13a** showed the same time- and dose-dependent responses as observed with ZINC13407541, but the magnitude of the increase in

serum phosphate levels in *Hyp* mice 4 hours after dosing was greater with **13a**, consistent with its improved IC_{50} (Fig. 5, A and B). At 100 mg/kg, **13a** almost completely corrected the phosphate levels of *Hyp* mice. No changes were observed in serum calcium in *Hyp* mice after its administration (Fig. 5, C and D). We observed a transient increase in FGF23 levels at 8 hours in response to single administration of compound **13a** (100mg/kg) (Fig. 5E), but levels return to baseline by 24 hours. At the 4 hours' time-point, when different doses of compound **13a** were compared, there were no changes in

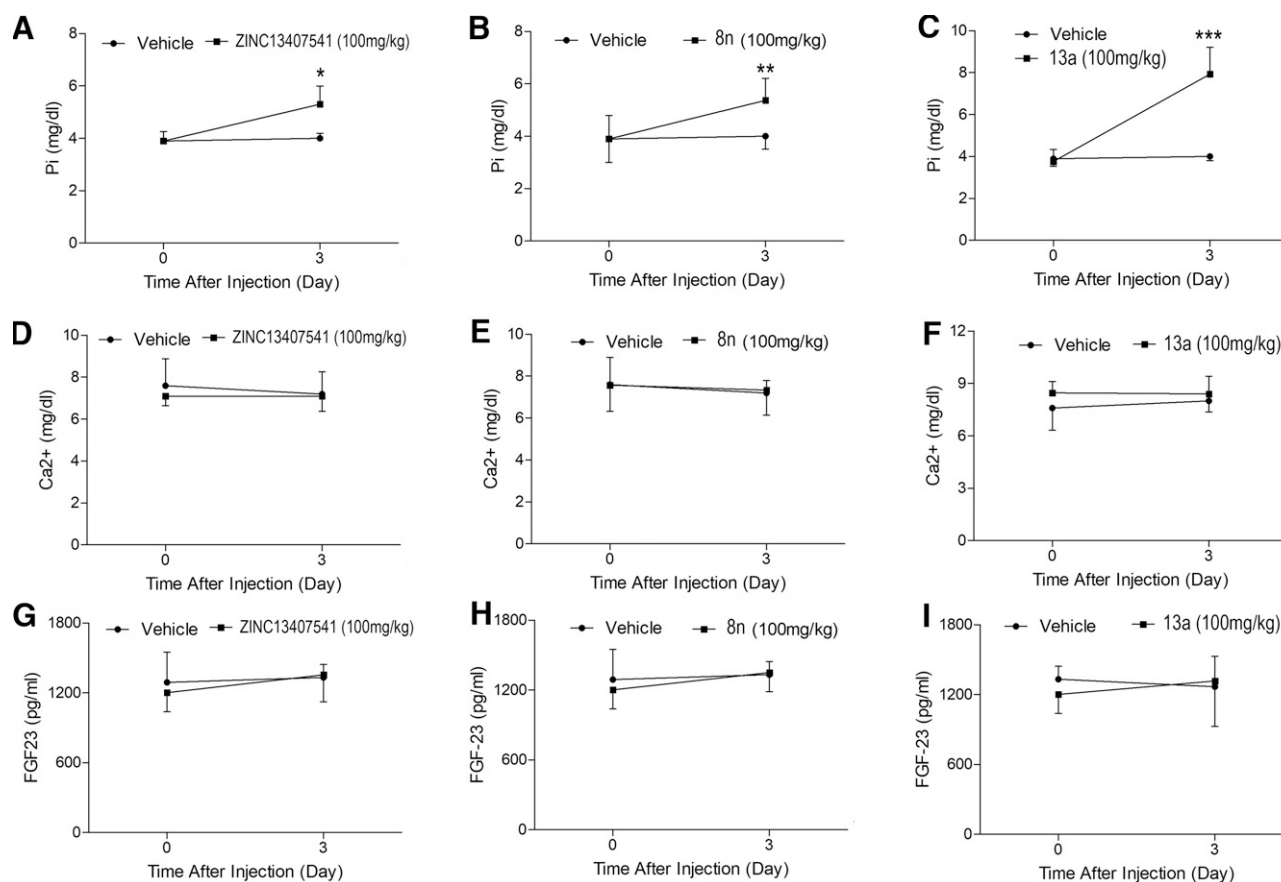


Fig. 6. Short-term effects of ZINC13407541, **8n**, and **13a** on mineral ion homeostasis and FGF23 levels in *Hyp* mice. (A–C) Serum phosphate. (D–F) Serum calcium. (G–I) Serum FGF23. Data are expressed as the mean \pm S.D. from serum samples of individual mice ($n = 5$). *, **, and *** indicate statistically significant difference from vehicle control group. *P* values were determined by two-way ANOVA with Bonferroni post hoc test.

serum FGF23 levels in *Hyp* mice (Fig. 5F). We also performed additional short-term treatments with ZINC 13407541 (100 mg/kg), **8n** (100 mg/kg), or **13a** (100 mg/kg) i.p. injection twice a day for 3 days. We observed similar effects of these three compounds to increase serum phosphate levels in *Hyp* mice (Fig. 6, A and B). No changes in serum calcium or FGF23 levels were observed with this treatment regimen in *Hyp* mice (Fig. 6, C–F).

Finally, to measure serum biochemistry and skeletal phenotype changes of *Hyp* mice treated with FGF23 inhibitors, we performed long-term exposure studies using half the effective dose (50 mg/kg) of ZINC13407541, **8n**, and **13a** as i.p.

injection twice a day for 4 weeks in *Hyp* mice. Four- to 8-week-old *Hyp* mice were administered with vehicle as a control or treated with either ZINC13407541 (50mg/kg), **8n** (50mg/kg), or **13a** (50mg/kg) for 4 weeks followed by measurement of serum biochemistry and assessment of skeletal parameters. Serum biochemistry measurements showed that serum phosphate levels were elevated in all FGF23 antagonist treated groups compared with vehicle controls. The increase in serum phosphate was relevant greater in **13a**, compared with ZINC13407541 and **8n** treated mice. No statistically significant changes of FGF23 levels were observed in **8n** and **13a** treated groups, compared with vehicle treated

TABLE 3

Serum biochemistry of *Hyp* mice treated with ZINC13407541 and its analogs

Data are expressed as the mean \pm S.D. from serum samples of individual mice ($n = 5$ –8). *, **, and *** indicate statistically significant difference from vehicle control group. *P* values were determined by one-way ANOVA with Tukey's multiple-comparisons test.

Parameters	Vehicle ($n = 7$)	ZINC13407541 ($n = 8$)	8n ($n = 8$)	13a ($n = 5$)	<i>p</i> -Value
FGF23 (pg/ml)	1413 \pm 366	2359 \pm 861*	1754 \pm 445	1378 \pm 289	0.0110
Phosphate (mg/dl)	4.6 \pm 0.60	6.5 \pm 1.02**	6.7 \pm 0.58**	7.8 \pm 1.08***	<0.0001
Calcium (mg/dl)	8.0 \pm 1.23	8.9 \pm 1.22	8.4 \pm 1.77	8.3 \pm 1.63	0.7208
PTH (pg/ml)	78 \pm 12	122 \pm 21**	118 \pm 20**	138 \pm 21***	0.0002
1,25(OH) ₂ D (pg/ml)	19 \pm 13	65 \pm 14***	69 \pm 19***	116 \pm 14***	<0.0001
Aldosterone (pg/ml)	278 \pm 84	389 \pm 68*	401 \pm 113*	497 \pm 71***	0.0031

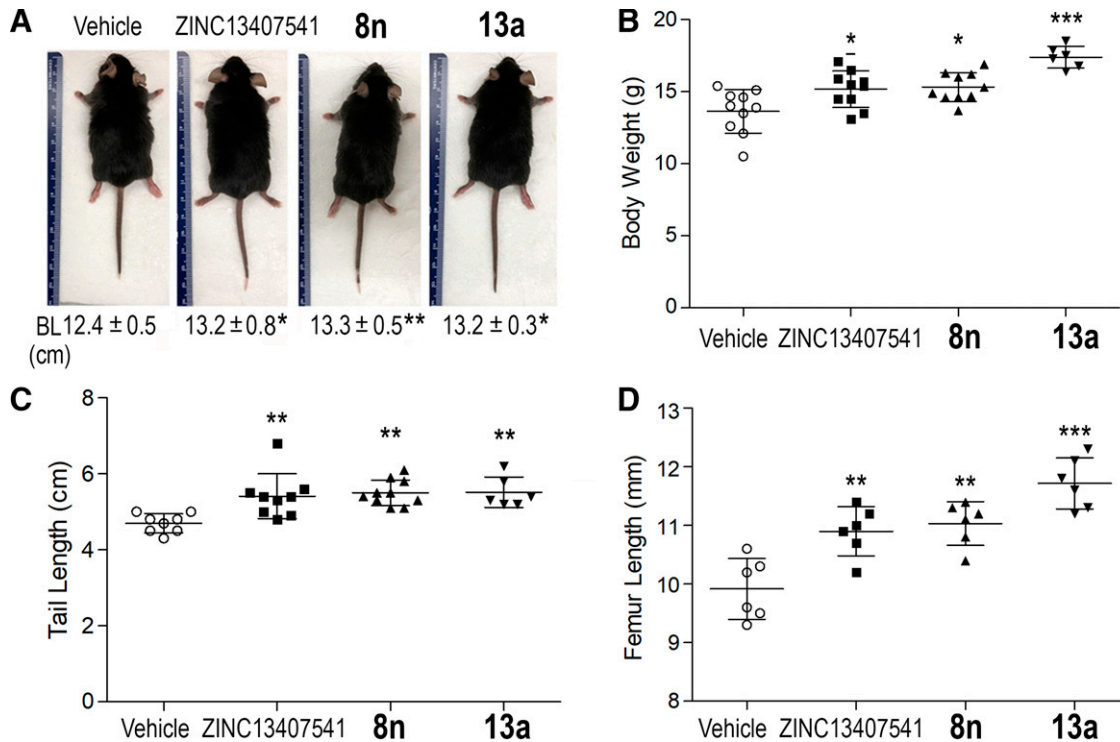


Fig. 7. Long-term effects of ZINC13407541, 8n, and 13a on skeletal phenotypes in *Hyp* mice. (A) body length ($n = 6-10$). (B) body weight ($n = 6-10$). (C) tail length ($n = 6-10$). (D) femur length ($n = 6$). Data are expressed as the mean \pm S.D. from serum samples of individual mice. *, **, and *** indicate statistically significant difference from vehicle control group. P values were determined by one-way ANOVA with Tukey's multiple-comparisons test.

mice (Table 3). There was a 1.5-fold increase of FGF23 in the ZINC13407541 treated group, similar to previous observations (Xiao et al., 2016). PTH and $1,25(\text{OH})_2\text{D}$ levels were increased in mice treated with ZINC13407541, 8n, or 13a (Xiao et al., 2018, 2019). FGF23 also has distal tubular effects to increase sodium reabsorption lead to suppression of aldosterone levels (Andrukhova et al., 2014; Han et al., 2016). ZINC13407541, 8n, and 13a resulted in stimulation in aldosterone levels compared with vehicle treated mice (Table 3), consistent with the inhibition of distal tubule effects of FGF23. With regard to skeletal effects, we observed that body weight, body length, femur length, and tail length were increased in *Hyp* mice treated with in ZINC13407541, 8n, or 13a compared with vehicle controls at the end of the treatment period (Fig. 7, A–D). *Hyp* mice treated with ZINC13407541, 8n, or 13a showed 15%, 18%, and 30% increments in femoral BMD, respectively, compared with vehicle controls (Fig. 8A). Micro-CT 3D images revealed that both ZINC13407541 and 8n treated groups had similar increases in trabecular bone volume, 51%, and Ct.Th, 30%. The *Hyp* mice treated with 13a had greater increases in both trabecular bone volume, 78%, and Ct.Th (44%) than either ZINC13407541 or 8n group (Fig. 8B). The width of the growth plate was reduced after treatment with ZINC13407541, 8n, or 13a. In summary, 13a had greater therapeutic effects on the healing of the growth plate in *Hyp* mice (Fig. 8B).

To further explore the gene expression profiles changes in bone of *Hyp* mice, we performed a real-time RT-PCR analysis from long bone samples treated long term with FGF23 inhibitors. *Hyp* mice have a distinct gene expression profile in bone associated with the presence of rickets/osteomalacia (Liu et al.,

2009; Martin et al., 2011; Xiao et al., 2014; Murali et al., 2016; Takashi et al., 2021). Real-time RT-PCR revealed that the antagonist-treated groups reduced FGFs/FGFRs-dependent signaling including *Fgf1*, *Fgf2*, *Fgf23*, *Fgfr1*, *Fgfr2*, *Fgfr3*, and *Fgfr4* expressions in bone as well as attenuated wingless (*Wnt*)/ β -catenin signaling, as evidence by reductions in *Wnt10b* and *axis inhibition protein 2* (*Axin 2*) (Table 4). Reduction in expression of osteoblast message levels for *Type 1 collagen*, *alkaline phosphatase* (*ALP*), and *dentin matrix protein 1* (*Dmp1*) were also observed in bone treated with ZINC13407541 and its analogs (Table 4). In contrast, mature osteoblast (Ob) markers, such as *matrix extracellular phosphoglycoprotein* (*MEPE*) and *Osteocalcin* and chondrocyte markers *Type2 collagen* but not *vascular endothelial growth factor A* (*VegfA*) were upregulated in femurs from the antagonists' treated groups. In addition, adipocyte markers *peroxisome proliferator-activated receptor gamma 2* (*Ppar γ 2*) *adipocyte fatty acid-binding protein 2* (*aP2*), and *lipoprotein lipase* were downregulated in all antagonists' treated groups (Table 4). The group treated with 13a had greater effects in all gene expressed markers than did either ZINC13407541 or the 8n group. However, there were no obvious changes in osteoclast markers, including *osteoprotegerin* (*OPG*), *receptor activator of nuclear factor kappa B ligand* (*RankL*), *matrix metalloproteinase 9* (*Mmp9*), and *tartrate-resistant acid phosphatase* (*Trap*) transcripts in the treated groups as compared with vehicle treated controls (Table 4).

We also examined the renal FGF23 signaling changes in kidney of *Hyp* mice treated long-term with FGF23 inhibitors. We previously reported that *Hyp* mice have a characteristic

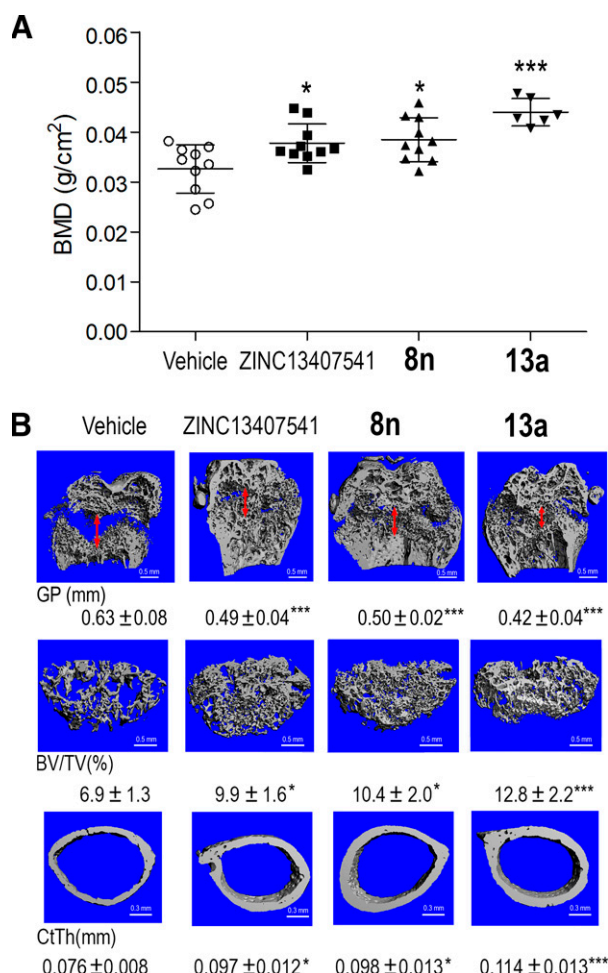


Fig. 8. Long-term effects of ZINC13407541, **8n**, and **13a** on bone mineral density and bone structure in *Hyp* mice. (A) BMD ($n = 6-10$). (B) Micro-CT 3D images, including width of the growth plate (GP, double red arrow, $n = 6$), femoral bone volume (BV/TV, $n = 6$), and cortical thickness (Ct.Th, $n = 6$). Data are expressed as the mean \pm S.D. from serum samples of individual mice ($n = 5$). *, **, and *** indicate statistically significant difference from vehicle control group. P values were determined by one-way ANOVA with Tukey's multiple-comparisons test.

gene expression profile in the kidney (Dai et al., 2012). Four weeks of treatment with FGF23 inhibitors altered FGF23 responsive gene expression in kidney of *Hyp* mice (Table 5). Compared with ZINC13407541 and **8n** groups, **13a** exhibited greater effects to increase *type IIa sodium phosphate co-transporter (Npt2a)* and *Npt2c* message expression, consistent with higher serum phosphate levels in the **13a** treated groups. Consistent with FGF23 stimulation of *cytochrome P450 family 27 subfamily b member 1 (Cyp27b1)*, and inhibition of *Cyp24a1*, leading to reductions in circulating 1,25(OH)₂D, the administration of ZINC13407541 and its analogs to *Hyp* mice increased the serum concentration of 1,25(OH)₂D (Table 3), in association with increased *Cyp27b1* and decreased *Cyp24a1* message expression (Table 5). FGF23 also stimulates *sodium-chloride co-transporter (NCC)* expression in the distal renal tubule cells leading to increased sodium (Na⁺) and potassium (K⁺) channel activity, sodium retention, and suppression of serum aldosterone. ZINC13407541, **8n**, and **13a** treatment suppressed NCC expression (Table 5), in association

with increased circulating aldosterone levels in *Hyp* mice. In contrast, treatment with ZINC13407541, **8n**, and **13a** had no effects on *Fgfr1* expression, but increased *Klotho* transcripts in kidney of *Hyp* mice (Table 3). These data indicate that ZINC13407541 and its analogs may have clinical utility in blocking the renal effects of excess FGF23.

Discussion

In this study, we are pursuing the development of small molecules that bind to FGF23 and inhibit its activation of the FGFRs/ α -Klotho binary receptor complex. Herein, we used a new 3D cryo-electron microscopy structure model to redock the FGF23 antagonists we identified in previous work (Xiao et al., 2016; Chen et al., 2018). We identified a key binding residue (Q156) of the FGF23 antagonists and developed a BiFC-based and ratiometric FRET assay to confirm that a series of small molecule FGF23 antagonists binding to Q156 based on the ZINC13407541 platform disrupt formation of the FGF23/ α -KL/FGFR1 triple complex (Tian et al., 2007; Shyu et al., 2008a, 2008b). Furthermore, we report on the efficacy of ZINC13407541 derivatives that displayed either greater stability (**8n**) in in vitro microsomal assays or greater potency (**13a**) in in vitro functional assays in a preclinical mouse model. Indeed, two compound **8n** and **13a** (most potent) demonstrated short- and long-term efficacy in blocking FGF23 end-organ effects in *Hyp* mice, a human homolog of XLH. We found that pharmacological inhibition of FGF23 efficiently abrogates aberrant FGF23 signaling, corrects hypophosphatemia and aberrant 1,25(OH)₂D levels, and improves both bone and renal gene expression profiles caused by elevated FGF23 levels in *Hyp* mice.

We observed that these small molecule FGF23 inhibitors antagonized both the proximal and distal tubular effects of FGF23 excess in *Hyp* mice in vivo. Increases in serum phosphate levels were observed as early as 3 to 5 hours after intraperitoneal injections of these compounds at a minimum effective dose was 50 mg/kg body weight, consistent with FGF23 regulation of phosphate metabolism in the kidneys. Long-term FGF23 inhibition with **8n** and **13a** treatment of *Hyp* mice for 4 weeks resulted in sustained increases in serum phosphate and 1,25(OH)₂D levels, enhanced bone growth, increased bone mineralization, and improvement of the rachitic growth plate abnormalities, in accordance with FGF23 regulation of vitamin D metabolism in kidney and bone homeostasis in vivo. Indeed, the improvement in biochemistries in *Hyp* mice after treatment with these chemical FGF23 inhibitors was associated with reversal of FGF23's renal effects on phosphate transporters and enzymes regulating vitamin D metabolism, including reversal of elevated FGF23 effects to suppresses the phosphate transporters *Npt2a* and *Npt2c* and *Cyp27b1* the enzyme that 1-hydroxylates 25-hydroxyvitamin D [25-(OH)D], and to stimulate *Cyp24a1*, which degrades 1,25(OH)₂D in the proximal tubule. The effects of excess FGF23 in *Hyp* mice stimulate the sodium chloride cotransporter in the distal tubule that leads to sodium retention and suppression of aldosterone (Xiao et al., 2019). Treatment with **8n** and **13a** reversed the excess FGF23 mediated renal tubule effects. In addition, treatment with **8n** and **13a** also increased α -Klotho transcript levels in *Hyp* mice. Although we did not test the effects of our compounds on blood pressure and cardiovascular effects of excess

TABLE 4

Gene-expression profiles in bone of *Hyp* mice treated with ZINC13407541 and its analogs
Data are expressed as the fold changes relative to the housekeeping gene β -actin subsequently normalized to control mice (n = 5–7). *, **, and *** indicate statistically significant difference from vehicle control group. *P* values were determined by one-way ANOVA with Tukey's multiple-comparisons test.

Gene	Vehicle (n = 6)	ZINC13407541 (n = 6)	8n (n = 7)	13a (n = 5)	<i>p</i> -Value
Osteoblast lineage					
<i>Fgfr1</i>	1.00 ± 0.35	0.51 ± 0.20**	0.56 ± 0.23**	0.21 ± 0.07***	0.0001
<i>Fgfr2</i>	1.00 ± 0.12	0.98 ± 0.29	0.94 ± 0.32	0.44 ± 0.06**	0.0010
<i>Fgfr3</i>	1.00 ± 0.25	1.14 ± 0.24	1.16 ± 0.21	0.42 ± 0.17***	<0.0001
<i>Fgfr4</i>	1.00 ± 0.59	0.53 ± 0.25*	0.45 ± 0.19**	0.25 ± 0.06***	0.0057
<i>Fgf1</i>	1.00 ± 0.25	1.14 ± 0.40	1.01 ± 0.39	0.38 ± 0.15*	0.0019
<i>Fgf2</i>	1.00 ± 0.32	1.04 ± 0.31	1.01 ± 0.27	0.52 ± 0.16*	0.0081
<i>Fgf23</i>	1.00 ± 0.33	0.88 ± 0.18	0.93 ± 0.41	0.46 ± 0.15*	0.0189
<i>Dmp1</i>	1.00 ± 0.48	0.77 ± 0.18	0.88 ± 0.16	0.38 ± 0.16***	0.0002
<i>Osteopontin</i>	1.00 ± 0.25	0.55 ± 0.11**	0.56 ± 0.16**	0.64 ± 0.12***	<0.0001
<i>Bsp</i>	1.00 ± 0.34	0.87 ± 0.27	0.95 ± 0.29	0.90 ± 0.18	0.8607
<i>Mepe</i>	1.00 ± 0.16	1.68 ± 0.35*	1.86 ± 0.44*	5.42 ± 0.77***	<0.0001
<i>Col1</i>	1.00 ± 0.28	0.55 ± 0.16**	0.62 ± 0.23*	0.30 ± 0.10***	<0.0001
<i>Alp</i>	1.00 ± 0.26	0.66 ± 0.20*	0.60 ± 0.19**	0.36 ± 0.08***	0.0001
<i>Osteocalcin</i>	1.00 ± 0.27	1.06 ± 0.32	1.25 ± 0.39	3.36 ± 0.97***	<0.0001
<i>Runx2-II</i>	1.00 ± 0.23	0.82 ± 0.41	0.91 ± 0.31	0.21 ± 0.11***	0.0003
<i>Opg</i>	1.00 ± 0.20	1.02 ± 0.33	0.96 ± 0.29	0.92 ± 0.37	0.9488
<i>RankL</i>	1.00 ± 0.16	0.85 ± 0.18	0.97 ± 0.37	0.87 ± 0.11	0.6112
<i>Fzd2</i>	1.00 ± 0.38	0.51 ± 0.21**	0.62 ± 0.16*	0.17 ± 0.08***	<0.0001
<i>Wnt10b</i>	1.00 ± 0.27	0.53 ± 0.24**	0.64 ± 0.16*	0.12 ± 0.06***	<0.0001
<i>Axin2</i>	1.00 ± 0.25	0.57 ± 0.21**	0.67 ± 0.17*	0.11 ± 0.06***	<0.0001
Osteoclast					
<i>Trap</i>	1.00 ± 0.17	0.91 ± 0.24	1.08 ± 0.27	0.86 ± 0.22	0.3383
<i>Mmp9</i>	1.00 ± 0.21	0.81 ± 0.39	1.10 ± 0.34	1.11 ± 0.13	0.2358
Chondrocyte					
<i>Collagen II</i>	1.00 ± 0.45	3.72 ± 1.08*	3.43 ± 2.27*	14.4 ± 2.65***	<0.0001
<i>VegfA</i>	1.00 ± 0.38	0.83 ± 0.51	0.77 ± 0.48	0.81 ± 0.27	0.7852
Adipocyte					
<i>PPARγ2</i>	1.00 ± 0.32	0.43 ± 0.29**	0.48 ± 0.31*	0.10 ± 0.08***	0.0001
<i>aP2</i>	1.00 ± 0.13	0.78 ± 0.15*	0.70 ± 0.16**	0.23 ± 0.11***	<0.0001
<i>Lpl</i>	1.00 ± 0.34	0.47 ± 0.23**	0.54 ± 0.24*	0.17 ± 0.07***	<0.0001

aP2, adipocyte fatty acid-binding protein 2; *Bsp*, bone sialoprotein; *Col1*, type I collagen; *Fzd2*, frizzled class receptor 2; *Lpl*, lipoprotein lipase; *Mmp9*, matrix metallo-peptidase 9; *Opg*, osteoprotegerin; *PPAR γ 2*, peroxisome proliferator-activated receptor gamma 2; *RankL*, receptor activator of nuclear factor kappa B ligand; *Runx2-II*, type II runt-related transcription factor-2; *Trap*, tartrate-resistant acid phosphatase; *VegfA*, vascular endothelial growth factor A.

FGF23, these results suggest possible beneficial effects of these small molecule inhibitors. Compared with compound ZINC13407541 and 8n, 13a had greater therapeutic effects on FGF23-induced abnormalities in *Hyp* mice, consistent with its lower IC₅₀.

Excess FGF23 has both indirect effects on bone and cartilage mineralization mediated by the reductions in serum phosphate and 1,25(OH)₂D (Liu et al., 2006, 2008), as well as possible direct effects due to FGF23 activation of FGFRs in osteoblasts (Shalhoub et al., 2011; Meng et al., 2020). We observed substantial improvement in bone abnormalities after only 4 weeks

of treatment as well as alteration in gene expression profiles in bone. Treatment with 8n and 13a altered osteoblast function as evidence by decreased *type II runt-related transcription factor-2 (Runx2-II)*, *alkaline phosphatase (Alp)*, *type I collagen (Col1)*, *osteopontin (Opn)* (Hoac et al., 2020), and *Dmp1* and increased *Mepe*, *bone sialoprotein (Bsp)*, and *Osteocalcin* expressions. FGF23 may also have effects on adipocytes to modulate adipogenesis (Xiao et al., 2019). This may explain the effects of FGF23 antagonists in reducing adipogenic markers in *Hyp* bone. Treatment with 8n and 13a reduced several *Fgfs/Fgfrs*, *Wnt10b*, *frizzled class receptor 2 (Fzd2)*, and *Axin2* gene

TABLE 5

Gene-expression profiles in kidney of *Hyp* mice treated with ZINC13407541 and its analogs (n = 5–6)
Data are expressed as the fold changes relative to the housekeeping gene β -actin subsequently normalized to control mice. *, **, and *** indicate statistically significant difference from vehicle control group. *P* values were determined by one-way ANOVA with Tukey's multiple-comparisons test.

Gene	Vehicle (n = 6)	ZINC13407541 (n = 6)	8n (n = 6)	13a (n = 5)	<i>p</i> -Value
<i>Fgfr1</i>	1.00 ± 0.19	0.98 ± 0.15	0.95 ± 0.13	0.90 ± 0.29	0.8270
<i>Npt2a</i>	1.00 ± 0.10	1.36 ± 0.15*	1.44 ± 0.19*	1.76 ± 0.44***	0.0007
<i>Npt2c</i>	1.00 ± 0.13	1.37 ± 0.15*	1.41 ± 0.11**	1.98 ± 0.48***	<0.0001
<i>Klotho</i>	1.00 ± 0.12	1.32 ± 0.16*	1.34 ± 0.16*	1.66 ± 0.22***	<0.0001
<i>Cyp24a1</i>	1.00 ± 0.10	0.69 ± 0.15**	0.64 ± 0.11***	0.66 ± 0.16***	0.0004
<i>Cyp27b1</i>	1.00 ± 0.10	1.42 ± 0.14*	1.48 ± 0.14*	2.08 ± 0.61***	0.0001
<i>NCC</i>	1.00 ± 0.15	0.64 ± 0.13***	0.72 ± 0.17**	0.55 ± 0.12***	0.0002

transcripts, consistent with our previous findings that *Hyp* mice exhibited higher *Fgfs/Fgfrs* and Wnt signaling (Liu et al., 2009; Xiao et al., 2014; Murali et al., 2016; Takashi et al., 2021). Increased FGF23 levels were observed in response to single administration of ZINC13407541 and compound **13a**, although the response of **13a** was transient. Similarly, treatment with ZINC13407541 for 4 weeks resulted in statistically significant increase in serum FGF23, but treatment with **8n** and **13a** did not increase the *FGF23* transcripts and serum FGF23 levels in *Hyp* mice. Changes in FGF23 may be compensating for the inhibition of FGF23 signaling, similar to the observed increase in serum FGF23 levels after treatment of patients with XLH with FGF23 blocking antibodies (https://www.ultragenyx.com/file.cfm/95/docs/Crysvita_Full_Prescribing_Information.pdf).

The short half-life of small molecules may be of considerable clinical benefit in titrating and reversing drug effects, which may be particularly important given the narrow therapeutic window for FGF23 suppression, particularly in chronic kidney disease (CKD). Preclinical CKD models show that inhibiting FGF23 with a blocking antibody increases mortality due to oversuppression of FGF23 (Shalhoub et al., 2012). Drawing analogies to treatment of secondary hyperparathyroidism with short acting calcimimetics in CKD to lower PTH levels and pointing to data that even partial reductions of FGF23 may be sufficient to reduce cardiovascular effects, a short-acting, titratable FGF23 antagonist might reduce FGF23 dose-dependent cardiotoxicity with acceptable side effects in CKD (Quarles, 2003, 2012; Weber et al., 2003). Further studies are needed to test the effects of these small molecules in models of CKD.

In conclusion, these studies further advance the premise that the development of FGF23 small molecule inhibitors is feasible for treatment of FGF23-mediated hypophosphatemic diseases and possibly other adverse effects of excess FGF23. Small molecules are generally more cost-effective, have a longer shelf life, and are more easily manufactured. In addition, the potential to modify our leads to develop an oral anti-FGF23 therapy has the potential to simplify the administration of FGF23 antagonists. Further lead optimization of these compounds is warranted to increase their drug-like properties and reduce their potential off-target effects.

Authorship Contributions

Participated in research design: Xiao, Carrick, Smith, Quarles.
Conducted experiments: Xiao, J.W. Liu, Cai, Cao, Wang, Chin, Cleveland, Ikedionwu.
Contributed new reagents or analytic tools: Xiao, J.W. Liu, Carrick.
Performed data analysis: Xiao, S.H. Liu, Petridis, Smith, Quarles.
Wrote or contributed to the writing of the manuscript: Xiao, S.H. Liu, Petridis, Carrick, Smith, Quarles.

References

- Andruchova O, Slavic S, Smorodchenko A, Zeitz U, Shalhoub V, Lanske B, Pohl EE, and Erben RG (2014) FGF23 regulates renal sodium handling and blood pressure. *EMBO Mol Med* 6:744–759 DOI: <https://doi.org/10.1002/emmm.201303716>.
- Arango Sancho P (2020) Complications of phosphate and vitamin D treatment in X-linked hypophosphatemia. *Adv Ther* 37 (Suppl 2):105–112 DOI: <https://doi.org/10.1007/s12325-019-01170-7>.
- Ashkenazy H, Abadi S, Martz E, Chay O, Mayrose I, Pupko T, and Ben-Tal N (2016) ConSurf 2016: an improved methodology to estimate and visualize evolutionary conservation in macromolecules. *Nucleic Acids Res* 44:W344–350 DOI: <https://doi.org/10.1093/nar/gkw408>.
- Carpenter TO, Imel EA, Ruppe MD, Weber TJ, Klausner MA, Wooddell MM, Kawakami T, Ito T, Zhang X, Humphrey J, et al. (2014) Randomized trial of the anti-FGF23 antibody KRN23 in X-linked hypophosphatemia. *J Clin Invest* 124:1587–1597 DOI: <https://doi.org/10.1172/JCI12829>.
- Carpenter TO, Whyte MP, Imel EA, Boot AM, Högl W, Linglart A, Padidela R, Van't Hoff W, Mao M, Chen CY, et al. (2018) Burosumab therapy in children with X-linked hypophosphatemia. *N Engl J Med* 378:1987–1998 DOI: <https://doi.org/10.1056/NEJMoa1714641>.
- Chen G, Liu Y, Goetz R, Fu L, Jayaraman S, Hu MC, Moe OW, Liang G, Li X, and Mohammadi M (2018) α -Klotho is a non-enzymatic molecular scaffold for FGF23 hormone signalling. *Nature* 553:461–466 DOI: <https://doi.org/10.1038/nature25451>.
- Colares Neto GP, Ide Yamauchi F, Hueb Baroni R, de Andrade Bianchi M, Cavalanti Gomes A, Chammass MC, and Matsunaga Martin R (2019) Nephrocalcinosis and nephrolithiasis in X-linked hypophosphatemic rickets: diagnostic imaging and risk factors. *J Endocr Soc* 3:1053–1061 DOI: <https://doi.org/10.1210/je.2018-00338>.
- Dai B, David V, Martin A, Huang J, Li H, Jiao Y, Gu W, and Quarles LD (2012) A comparative transcriptome analysis identifying FGF23 regulated genes in the kidney of a mouse CKD model. *PLoS One* 7:e44161 DOI: <https://doi.org/10.1371/journal.pone.0044161>.
- Downs RP, Xiao Z, Ikedionwu MO, Cleveland JW, Lin Chin A, Cafferty AE, Darryl Quarles L, and Carrick JD (2021) Design and development of FGF-23 antagonists: definition of the pharmacophore and initial structure-activity relationships probed by synthetic analogues. *Bioorg Med Chem* 29:115877 DOI: <https://doi.org/10.1016/j.bmc.2020.115877>.
- Ellingson SR, Smith JC, and Baudry J (2013) VinaMPI: facilitating multiple receptor high-throughput virtual docking on high-performance computers. *J Comput Chem* 34:2212–2221 DOI: <https://doi.org/10.1002/jcc.23367>.
- Florenzano P, Gafni RI, and Collins MT (2017) Tumor-induced osteomalacia. *Bone Rep* 7:90–97 DOI: <https://doi.org/10.1016/j.bonr.2017.09.002>.
- Fukumoto S (2014) Diagnostic modalities for FGF23-producing tumors in patients with tumor-induced osteomalacia. *Endocrinol Metab (Seoul)* 29:136–143 DOI: <https://doi.org/10.3803/EnM.2014.29.2.136>.
- Fukumoto S (2018) Targeting fibroblast growth factor 23 signaling with antibodies and inhibitors, is there a rationale? *Front Endocrinol (Lausanne)* 9:48 DOI: <https://doi.org/10.3389/fendo.2018.00048>.
- Gutiérrez OM, Januzzi JL, Isakova T, Laliberte K, Smith K, Collerone G, Sarwar A, Hoffmann U, Coglianese E, Christenson R, et al. (2009) Fibroblast growth factor 23 and left ventricular hypertrophy in chronic kidney disease. *Circulation* 119:2545–2552 DOI: <https://doi.org/10.1161/CIRCULATIONAHA.108.844506>.
- Gutiérrez OM, Mannstadt M, Isakova T, Rauh-Hain JA, Tamez H, Shah A, Smith K, Lee H, Thadhani R, Jüppner H, et al. (2008) Fibroblast growth factor 23 and mortality among patients undergoing hemodialysis. *N Engl J Med* 359:584–592 DOI: <https://doi.org/10.1056/NEJMoa0706130>.
- Han X, Yang J, Li L, Huang J, King G, and Quarles LD (2016) Conditional deletion of Fgf1 in the proximal and distal tubule identifies distinct roles in phosphate and calcium transport. *PLoS One* 11:e0147845–67 DOI: <https://doi.org/10.1002/1873-3468.12040>.
- Hoac B, Østergaard M, Wittig NK, BoukpeSSI T, Buss DJ, Chaussain C, Birkedal H, Mørshed M, and McKee MD (2020) Genetic ablation of osteopontin in osteomalacic Hyp mice partially rescues the deficient mineralization without correcting hypophosphatemia. *J Bone Miner Res* 35:2032–2048 DOI: <https://doi.org/10.1002/jbmr.4101>.
- Hsu HJ and Wu MS (2009) Fibroblast growth factor 23: a possible cause of left ventricular hypertrophy in hemodialysis patients. *Am J Med Sci* 337:116–122.
- Humphrey W, Dalke A, and Schulten K (1996) VMD: visual molecular dynamics. *J Mol Graph* 14:33–38, 27–28 DOI: [https://doi.org/10.1016/0263-7855\(96\)00018-5](https://doi.org/10.1016/0263-7855(96)00018-5).
- Isakova T, Xie H, Yang W, Xie D, Anderson AH, Scialla J, Wahl P, Gutiérrez OM, Steigerwalt S, He J, et al. (2011) Chronic Renal Insufficiency Cohort (CRIC) Study Group (2011) Fibroblast growth factor 23 and risks of mortality and end-stage renal disease in patients with chronic kidney disease. *JAMA* 305:2432–2439 DOI: <https://doi.org/10.1001/jama.2011.826>.
- Jean G, Bresson E, Terrat JC, Vanel T, Hurot JM, Lorriaux C, Mayor B, and Chazot C (2009) Peripheral vascular calcification in long-haemodialysis patients: associated factors and survival consequences. *Nephrol Dial Transplant* 24:948–955.
- Jiménez J, Skalić M, Martínez-Rosell G, and De Fabritiis G (2018) K_{DEEP}: protein-ligand absolute binding affinity prediction via 3D-convolutional neural networks. *J Chem Inf Model* 58:287–296 DOI: <https://doi.org/10.1021/acs.jcim.7b00650>.
- Lamb YN (2018) Burosumab: first global approval. *Drugs* 78:707–714 DOI: <https://doi.org/10.1007/s40265-018-0905-7>.
- Laskowski RA and Swindells MB (2011) LigPlot+: multiple ligand-protein interaction diagrams for drug discovery. *J Chem Inf Model* 51:2778–2786 DOI: <https://doi.org/10.1021/ci200227u>.
- Liu S, Tang W, Fang J, Ren J, Li H, Xiao Z, and Quarles LD (2009) Novel regulators of Fgf23 expression and mineralization in Hyp bone. *Mol Endocrinol* 23:1505–1518 DOI: <https://doi.org/10.1210/me.2009-0085>.
- Liu S, Zhou J, Tang W, Jiang X, Rowe DW, and Quarles LD (2006) Pathogenic role of Fgf23 in Hyp mice. *Am J Physiol Endocrinol Metab* 291:E38–E49 DOI: <https://doi.org/10.1152/ajpendo.00008.2006>.
- Liu S, Zhou J, Tang W, Menard R, Feng JQ, and Quarles LD (2008) Pathogenic role of Fgf23 in Dmp1-null mice. *Am J Physiol Endocrinol Metab* 295:E254–E261 DOI: <https://doi.org/10.1152/ajpendo.90201.2008>.
- Martin A, Liu S, David V, Li H, Karydis A, Feng JQ, and Quarles LD (2011) Bone proteins PHEX and DMP1 regulate fibroblastic growth factor Fgf23 expression in osteocytes through a common pathway involving FGF receptor (FGFR) signaling. *FASEB J* 25:2551–2562 DOI: <https://doi.org/10.1096/fj.10.177816>.
- Meng F, Bertucci C, Gao Y, Li J, Lu S, LeBoff MS, Glowacki J, and Zhou S (2020) Fibroblast growth factor 23 counters vitamin D metabolism and action in human mesenchymal stem cells. *J Steroid Biochem Mol Biol* 199:105587 DOI: <https://doi.org/10.1016/j.jsbmb.2020.105587>.
- Murali SK, Andruchova O, Clinkenbeard EL, White KE, and Erben RG (2016) Excessive osteocytic Fgf23 secretion contributes to pyrophosphate accumulation and mineralization defect in Hyp mice. *PLoS Biol* 14:e1002427 DOI: <https://doi.org/10.1371/journal.pbio.1002427>.

- Qiu N, Xiao Z, Cao L, David V, and Quarles LD (2012a) Conditional mesenchymal disruption of *pkd1* results in osteopenia and polycystic kidney disease. *PLoS One* **7**:e46038 DOI: <https://doi.org/10.1371/journal.pone.0046038>.
- Qiu N, Zhou H, and Xiao Z (2012b) Downregulation of PKD1 by shRNA results in defective osteogenic differentiation via cAMP/PKA pathway in human MG-63 cells. *J Cell Biochem* **113**:967–976 DOI: <https://doi.org/10.1002/jcb.23426>.
- Quarles LD (2003) Evidence for a bone-kidney axis regulating phosphate homeostasis. *J Clin Invest* **112**:642–646 DOI: <https://doi.org/10.1172/JCI19687>.
- Quarles LD (2011) The bone and beyond: 'dem bones' are made for more than walking. *Nat Med* **17**:428–430 DOI: <https://doi.org/10.1038/nm0411-428>.
- Quarles LD (2012) Role of FGF23 in vitamin D and phosphate metabolism: implications in chronic kidney disease. *Exp Cell Res* **318**:1040–1048 DOI: <https://doi.org/10.1016/j.yexcr.2012.02.027>.
- Shalhoub V, Shatzen EM, Ward SC, Davis J, Stevens J, Bi V, Renshaw L, Hawkins N, Wang W, Chen C, et al. (2012) FGF23 neutralization improves chronic kidney disease-associated hyperparathyroidism yet increases mortality. *J Clin Invest* **122**:2543–2553 DOI: <https://doi.org/10.1172/JCI61405>.
- Shalhoub V, Ward SC, Sun B, Stevens J, Renshaw L, Hawkins N, and Richards WG (2011) Fibroblast growth factor 23 (FGF23) and alpha-klotho stimulate osteoblastic MC3T3.E1 cell proliferation and inhibit mineralization. *Calcif Tissue Int* **89**:140–150 DOI: <https://doi.org/10.1007/s00223-011-9501-5>.
- Shyu YJ, Suarez CD, and Hu CD (2008a) Visualization of AP-1 NF-kappaB ternary complexes in living cells by using a BiFC-based FRET. *Proc Natl Acad Sci USA* **105**:151–156 DOI: <https://doi.org/10.1073/pnas.0705181105>.
- Shyu YJ, Suarez CD, and Hu CD (2008b) Visualization of ternary complexes in living cells by using a BiFC-based FRET assay. *Nat Protoc* **3**:1693–1702 DOI: <https://doi.org/10.1038/nprot.2008.157>.
- Song P, Ma F, Wang F, Wang X, Patil R, Ramagiri S, Orr WE, Miller DD, Geisert E, and Yates CR (2008) Plasma and cerebrospinal fluid pharmacokinetics of the novel tetrahydroisoquinoline EDL-155 in rats. *Cancer Chemother Pharmacol* **61**:1037–1044.
- Stubbs JR, Liu S, Tang W, Zhou J, Wang Y, Yao X, and Quarles LD (2007) Role of hyperphosphatemia and 1,25-dihydroxyvitamin D in vascular calcification and mortality in fibroblastic growth factor 23 null mice. *J Am Soc Nephrol* **18**:2116–2124 DOI: <https://doi.org/10.1681/ASN.2006121385>.
- Takashi Y, Sawatsubashi S, Endo I, Ohnishi Y, Abe M, Matsuhisa M, Kawanami D, Matsumoto T, and Fukumoto S (2021) Skeletal FGFR1 signaling is necessary for regulation of serum phosphate level by FGF23 and normal life span. *Biochem Biophys Res Rep* **27**:101107 DOI: <https://doi.org/10.1016/j.bbrep.2021.101107>.
- Tian H, Ip L, Luo H, Chang DC, and Luo KQ (2007) A high throughput drug screen based on fluorescence resonance energy transfer (FRET) for anticancer activity of compounds from herbal medicine. *Br J Pharmacol* **150**:321–334 DOI: <https://doi.org/10.1038/sj.bjp.0706988>.
- Trott O and Olson AJ (2010) AutoDock Vina: improving the speed and accuracy of docking with a new scoring function, efficient optimization, and multithreading. *J Comput Chem* **31**:455–461 DOI: <https://doi.org/10.1002/jcc.21334>.
- Urakawa I, Yamazaki Y, Shimada T, Iijima K, Hasegawa H, Okawa K, Fujita T, Fukumoto S, and Yamashita T (2006) Klotho converts canonical FGF receptor into a specific receptor for FGF23. *Nature* **444**:770–774 DOI: <https://doi.org/10.1038/nature05315>.
- Webb B and Sali A (2014) Comparative Protein Structure Modeling Using MODELLER. *Curr Protoc Bioinformatics* **47**:1–32 DOI: <https://doi.org/10.1002/0471250953.bi0506s47>.
- Weber TJ, Liu S, Indridason OS, and Quarles LD (2003) Serum FGF23 levels in normal and disordered phosphorus homeostasis. *J Bone Miner Res* **18**:1227–1234 DOI: <https://doi.org/10.1359/jbmr.2003.18.7.1227>.
- Widom B (2002) *Statistical Mechanics: A Concise Introduction for Chemists*, Cambridge University Press, New York.
- Xiao L, Homer-Bouthiette C, and Hurley MM (2018) FGF23 neutralizing antibody partially improves bone mineralization defect of HMWFGF2 isoforms in transgenic female mice. *J Bone Miner Res* **33**:1347–1361 DOI: <https://doi.org/10.1002/jbmr.3417>.
- Xiao Z, Huang J, Cao L, Liang Y, Han X, and Quarles LD (2014) Osteocyte-specific deletion of *Fgfr1* suppresses FGF23. *PLoS One* **9**:e104154 DOI: <https://doi.org/10.1371/journal.pone.0104154>.
- Xiao Z, King G, Mancarella S, Munkhsaikhan U, Cao L, Cai C, and Quarles LD (2019) FGF23 expression is stimulated in transgenic α -Klotho longevity mouse model. *JCI Insight* **4**:132820 DOI: <https://doi.org/10.1172/jci.insight.132820>.
- Xiao Z, Riccardi D, Velazquez HA, Chin AL, Yates CR, Carriek JD, Smith JC, Baudry J, and Quarles LD (2016) A computationally identified compound antagonizes excess FGF-23 signaling in renal tubules and a mouse model of hypophosphatemia. *Sci Signal* **9**:ra113 DOI: <https://doi.org/10.1126/scisignal.aaf5034>.
- Xiao Z, Zhang S, Cao L, Qiu N, David V, and Quarles LD (2010) Conditional disruption of *Pkd1* in osteoblasts results in osteopenia due to direct impairment of bone formation. *J Biol Chem* **285**:1177–1187 DOI: <https://doi.org/10.1074/jbc.M109.050906>.
- Xiao Z, Zhang S, Magenheimer BS, Luo J, and Quarles LD (2008) Polycystin-1 regulates skeletogenesis through stimulation of the osteoblast-specific transcription factor RUNX2-II. *J Biol Chem* **283**:12624–12634 DOI: <https://doi.org/10.1074/jbc.M710407200>.
- Yamazaki Y, Tamada T, Kasai N, Urakawa I, Aono Y, Hasegawa H, Fujita T, Kuroki R, Yamashita T, Fukumoto S, et al. (2008) Anti-FGF23 neutralizing antibodies show the physiological role and structural features of FGF23. *J Bone Miner Res* **23**:1509–1518 DOI: <https://doi.org/10.1359/jbmr.080417>.
- Zeng K, Thompson KE, Presley CS, Miller DD, and Yates CR (2011) Preclinical pharmacokinetics of the radiomitigator KZ-41 in rats. *Xenobiotica* **41**:1006–1012 DOI: <https://doi.org/10.3109/00498254.2011.603387>.

Address correspondence to: Dr. Leigh Darryl Quarles, Coleman College of Medicine Building, Suite B216, University of Tennessee Health Science Center, 956 Court Avenue, Memphis TN 38163. E-mail: dquarles@uthsc.edu; or Dr. Zhousheng Xiao, University of Tennessee Health Science Center, 19S Manassas Street, CRB362, Memphis, TN, 38103. E-mail: zxiao2@uthsc.edu
